BOUNDARY LAYER TRANSITION MECHANISMS IN A HIGH-SPEED LOW-PRESSURE TURBINE BLADE

G. Lopes[1,3], *S. Lavagnoli*[1], *K. Hillewaert*[1,2,4], *M. Dellacasagrande*[3] *and D. Lengani*[3]

[1] *Turbomachinery Department, von Karman Institute for Fluid Dynamics*
[2] *Aerospace and Mechanics Department, University of Liège*
[3] *DIME, University of Genova*
[4] *Centre de recherche en Aéronautique (Cenaero)*

gustavo.lopes@vki.ac.be

Abstract

The suction side boundary layer regimes in a modern high-speed, low-pressure turbine cascade under off-design conditions are investigated using high-fidelity direct numerical simulations with the Argo DG solver on the SPLEEN C1 geometry at $Re_c = 70k$. Three outlet Mach numbers ($Ma = 0.70, 0.90, 0.95$) reveal a Kelvin-Helmholtz driven laminar separation bubble with tonal noise at $Ma = 0.70$, an acoustic interaction with the separation bubble that governs reattachment at $Ma = 0.90$, and a shock-dominated flow with passage normal shock modulation at $Ma = 0.95$. These results show how shear layer instabilities, acoustic waves, and shocks alter the suction side boundary layer across the flight envelope of a high-speed LPT.

1 Introduction

During cruise, low-pressure turbine blading in aeroengines is subjected to low Reynolds numbers, allowing the suction side (SS) boundary layer to remain laminar over a large portion of the blade. An adverse pressure gradient downstream of the velocity peak often leads to laminar separation. In this separated shear layer, small disturbances grow by a Kelvin-Helmholtz instability and roll up into vortices that enhance momentum transfer and can promote the occurrence of a laminar separation bubble (LSB) if reattachment occurs, as shown by Marxen and Henningson (2011) and Boutilier and Yarusevych (2012).

The shear layer roll-up vortices convect past the trailing edge plane and generate upstream-radiating acoustic waves that interact with the separation bubble, modulating its separation and reattachment dynamics, as demonstrated by Jones et al. (2010). Pröbsting et al. (2014) showed that the acoustic waves can shift the LSB separation point.

The trailing edge (TE) shedding regime depends on the Mach number, Reynolds number, and geometry. Rossiter et al. (2023) demonstrated that above a critical Reynolds number, upstream-traveling expansion waves and shocks form at the trailing edge, whereas at low Reynolds numbers, the shear layer detaches, and a recirculation zone appears in the trailing edge base region, thereby reducing losses. These results, obtained for high-pressure turbines and simplified models, do not directly apply to high-speed low-pressure turbines, where the effect of trailing edge shedding on the suction side boundary layer remains unexplored.

When operating off-design at higher Mach numbers, high-speed LPTs develop a passage normal shock that interacts unsteadily with the laminar separation bubble, as shown by Börner and Niehuis (2021). They identified a low frequency mode of shock–bubble modulation and a high frequency mode linked to shear layer mixing.

These phenomena can coexist across the flight envelope of high-speed low-pressure turbine blading, from takeoff to cruise, and strongly alter the suction side boundary layer behavior. This study examines how suction side boundary layer dynamics evolve with increasing Mach number in a modern high-speed LPT cascade by isolating the dominant unsteady interactions at on- and off-design conditions.

2 Numerical Setup

Direct numerical simulations were performed using the high-order discontinuous Galerkin code Argo-DG developed at Cenaero, which solves the compressible Navier–Stokes equations on unstructured meshes. This work builds on the open-access SPLEEN C1 test case described by Lavagnoli et al. (2023) and the DNS database first generated by Borbouse et al. (2025) using Argo-DG. A fourth order accurate interpolation was used, without shock-capturing. The spanwise extent of the blade is 7.5% of its axial chord. Three engine-representative outlet conditions are considered, all at $Re_c = 70k$, with $Ma = 0.70$, 0.90, and 0.95, based upon the true chord and an isentropic equivalent of the outlet conditions. The on-design point of the blade is at $Ma = 0.90$, $Re_c = 70k$. The suction side adverse pressure gradient (APG_{SS}) varies with the outlet Mach number for the fixed geometry. No turbulence was injected at the inlet, while the turbulence intensity (TI) and length scale (L_s/C) were surveyed at the inlet of the cascade between passages. Table 1

summarizes the flow conditions for each case.

Case	Ma	Re_c	APG_{SS}	TI	L_s/C
M070	0.70	70k	-0.14	0.42%	0.030
M090	0.90	70k	-0.08	0.01%	0.096
M095	0.95	70k	-0.06	0.01%	0.068

Table 1: Characterization of investigated cases

Figure 1 shows the streamwise and wall-normal viscous units along the suction side, confirming that the mesh resolves the boundary layer. Data was collected for more than 12 throughflow times (based on blade chord and outlet velocity) at a sampling frequency of 500 kHz, yielding 1281, 1242, and 1746 snapshots for $Ma = 0.70$, 0.90, and 0.95, respectively.

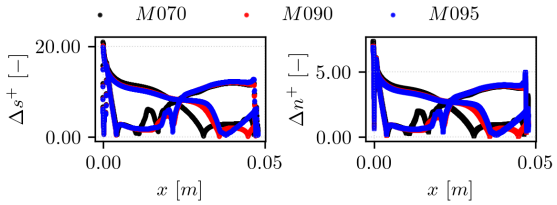

Figure 1: Streamwise and wall-normal viscous wall units.

3 Time mean aerodynamics

Figure 2 presents the suction side pressure coefficient $C_p = (P_{0,\mathrm{in}} - P_{\mathrm{blade}})/(P_{0,\mathrm{in}} - P_{\mathrm{out}})$, boundary layer shape factor H_{12}, and wall shear stress τ_w along the rear portion of the suction side surface arc-length. At $Ma = 0.70$ and 0.90, the adverse pressure gradient between $s/S = 0.60$ and 0.85 induces laminar separation bubbles: the plateau in C_p at $Ma = 0.70$ and the region of negative τ_w at $Ma = 0.90$ mark the separation–reattachment extent. At $Ma = 0.95$, τ_w approaches zero, but no mean separation occurs. The rise in H_{12} downstream of the velocity peak reflects displacement thickness growth.

The time-averaged numerical Schlieren in Figure 3 shows negligible compression at Ma = 0.70, a sonic pocket near the throat at Ma = 0.90, and a well-defined throat shock with reflections at Ma = 0.95.

Table 2 lists the normalized locations s/S of mean separation, reattachment, and shock (or compression fan) for each case.

Case	Sep.	Reatt.	Shock
M070	0.58	0.95	–
M090	0.69	0.91	0.67
M095	–	–	0.70

Table 2: Location, s/S, of flow features.

4 Instantaneous flow description

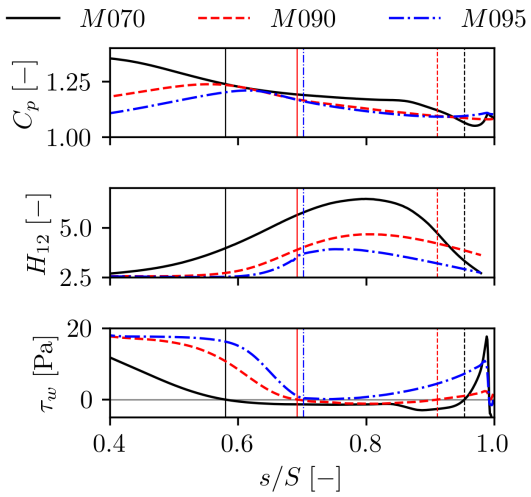

Figure 2: Time-mean SS metrics: shape factor H_{12}, pressure coefficient C_p, and wall shear stress τ_w.

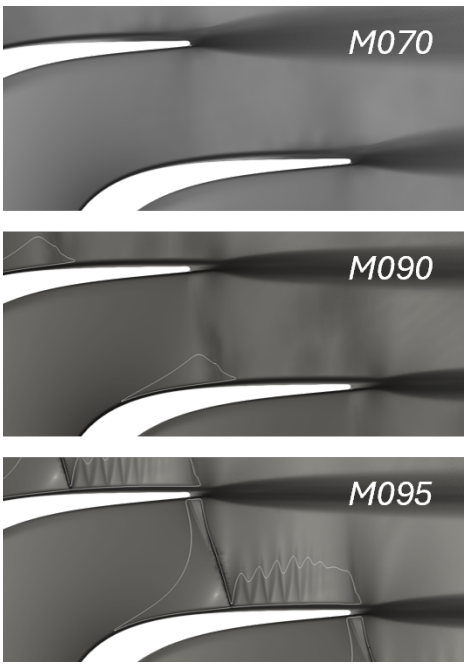

Figure 3: Time-averaged normalized density gradient inside the passage for Ma = 0.70, 0.90, 0.95.

Figure 4 presents instantaneous snapshots of the normalized density gradient $\|\nabla\rho\|/\rho$ for the three Mach numbers. At $Ma = 0.70$, the wake is irregular, with Kelvin-Helmholtz roll-ups creating local transonic pockets ($Ma < 1$) and weak, aperiodic pressure waves. At $Ma = 0.90$, the wake becomes periodic: well-defined pressure waves originate at the trailing edge, travel upstream along the suction side and accumulate near the throat, and supersonic cores appear within the shed vortices. At $Ma = 0.95$, these features intensify, and a clear cross-passage normal

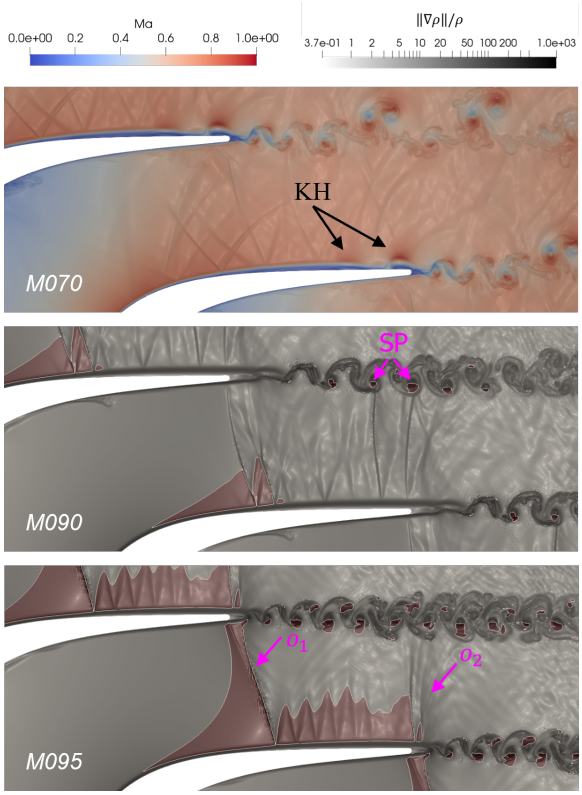

Figure 4: Instantaneous normalized density gradient for M070 (Mach contours 0-1), M090 and M095 (shaded for $Ma > 1$).

shock forms at the throat (o_1), with strong upstream-radiating pressure waves and a slight contraction near the trailing edge (o_2).

In Figure 5, the normalized PSD of u' and P' at z_2 (half the recirculation-zone height for $Ma = 0.70$ and 0.90 and at half the shear-layer thickness for $Ma = 0.95$) and z_4 (outside of shear layer) is plotted for $Ma = 0.70$, 0.90, and 0.95. The probes are located at the arc-length location of maximum shear layer thickness ($s/S = 0.91$ for M070 and 0.87 for M090 and M095). For each case, the dominant frequencies approximately differ by one order of magnitude. At $Ma = 0.70$, discrete peaks at $f \approx 14.4$ and 15.2 kHz in both u' and P' support tonal noise from roll-up vortices convecting past the trailing edge, in agreement with Pröbsting et al. (2014). At $Ma = 0.90$, only a 7.2 kHz peak appears, indicating weaker coupling between inner and outer shear-layer regions. At $Ma = 0.95$, two low-frequency peaks at 0.85 and 1.6 kHz dominate, reflecting unsteady shock dynamics. High-frequency inserts show energy at 46 kHz for M090 and 59–61 kHz for M095, linked to trailing-edge vortex shedding.

5 Proper orthogonal decomposition

Space-only proper orthogonal decomposition (POD) was applied to the instantaneous flowfields using the method of snapshots proposed by Sirovich

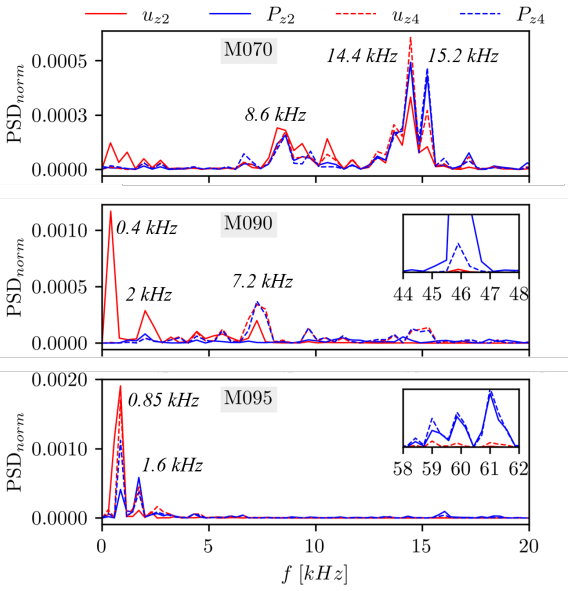

Figure 5: Normalized PSD of u' (red) and P' (blue) at z_2 (full) and z_4 (dashed) for $Ma = 0.70$, 0.90, and 0.95.

(1987):

$$\Phi = QX \tag{1}$$

Where Φ is the matrix containing the POD modes, $Q = [\rho\ u\ v\ w\ T]^T$ is the snapshot matrix built from an ensemble of observations stacked along the matrix columns, and X is the matrix containing the eigenvectors. Since the flow is compressible, the weight matrix proposed by Chu (1965), W, was used. The weight matrix ensures that the cross-correlation matrix $C = Q^T W Q$ induces the compressible energy norm:

$$W = \begin{bmatrix} \dfrac{\bar{c}^2}{\gamma\,\bar{\rho}} & & & & \\ & \bar{\rho} & & & \\ & & \bar{\rho} & & \\ & & & \bar{\rho} & \\ & & & & \dfrac{\bar{\rho}\,R}{\bar{T}(\gamma-1)} \end{bmatrix} \tag{2}$$

Figure 6 shows the relative modal energy $E_r^{(m)} = \lambda^{(m)} / \sum \lambda^{(m)}$ and its cumulative sum $E_c^{(m)}$ modal energy for each Mach case. At $Ma = 0.70$, the first two coupled modes capture over 50% of the energy, reflecting the dominant Kelvin–Helmholtz instability and acoustic feedback. At $Ma = 0.90$, the energy is spread over a broader set of modes, requiring 29 modes to reach 99% energy capture. At $Ma = 0.95$, the first mode alone captures nearly 50%, corresponding to unsteady shock modulation, with 102 modes needed for 99% capture. These modal highlights the presented in Figure 7, the dominant flow features with respect to the Mach number.

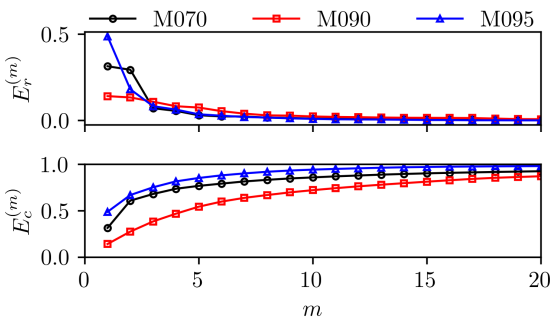

Figure 6: Relative and cumulative modal energy for $Ma = 0.70$, 0.90, and 0.95.

the mode number and Strouhal number $St_0 = f\,\theta_{\text{sep}}/U_{\text{sep}}$ computed with the boundary layer momentum thciknnes θ and the velocity U at the separation location. The approximate shock impinging location was used for M095. At $Ma = 0.70$, strong energy appears in the lowest modes at the K–H roll-up frequency, with trailing-edge shedding also captured by early modes. At $Ma = 0.90$, a nearly linear mode-frequency trend emerges, reflecting a broad range of interacting scales. At $Ma = 0.95$, a concentration of energy near the origin corresponds to unsteady shock modulation, with higher modes containing weaker acoustic feedback content. The signature of the trailing edge shed (TES) frequency, previously highlighted in Figure 5, is visible for lower modes at $Ma = 0.90$ and 0.95.

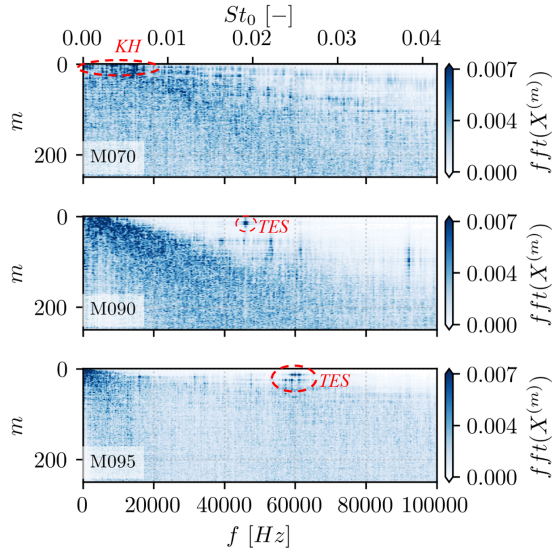

Figure 7: Spectrograms of FFT amplitude of POD temporal coefficients versus mode number and Strouhal number for Ma = 0.70, 0.90, and 0.95.

Following Lengani et al. (2017), low-rank reconstructions were formed by combining selected POD modes to isolate shear-layer roll-ups, acoustic waves, and shock dynamics. Figure 8 shows snapshots of u' reconstructed with increasing mode count. The dashed line encloses the recirculating region, and the dotted-dashed line marks the shear-layer thickness estimated using the procedure of Uzun and Malik (2020). The first row is the original field; each subsequent row considers a range of POD modes.

At $Ma = 0.70$, the first two modes recover the shear layer roll-ups. Modes 3–5 capture separation bubble modulation between $s/S = 0.60$ and 0.80 within the shear layer. The acoustic waves require over 200 modes, confirming their broadband nature.

At $Ma = 0.90$. Modes 1-2 highlight a strong link with the expansion wave region in the cascade throat. The first 20 modes reconstruct both the LSB modulation and upstream-traveling acoustic waves linked to trailing-edge shedding. A large modulated region between $s/S = 0.72$ and 0.98 within the shear layer supports the correlation between the LSB modulation and the system of acoustic waves. It suggests that the acoustic waves drive the laminar separation bubble reattachment in the absence of the typical shear-layer roll-ups induced by the K-H instability.

At $Ma = 0.95$, the first five modes capture the passage shock and its unsteady modulation. Adding up to 100 modes produces minimal further detail.

6 Characterization of instabilities

The time–space diagrams of u' in Figure 9 map the convection of the shear layer roll-ups and acoustic waves along the normalized suction side length s/S for ten throughflow periods. Diagrams use data at half the recirculation-zone height for $Ma = 0.70$ and 0.90 and at half the shear-layer thickness for $Ma = 0.95$. Separation and reattachment lines appear for Ma = 0.70 and 0.90, while the shock foot marks $Ma = 0.95$.

At $Ma = 0.70$, shear-layer roll-ups produce a forward-propagating trace starting at $s/S = 0.75$, and weaker backward-propagating waves extend from the mid-bubble to the velocity peak. At $Ma = 0.90$, only backward-propagating disturbances appear, and their amplitude decays sharply at the compression-fan impingement. At $Ma = 0.95$, incoherent backward-propagating disturbances persist up to the shock-impingement location.

The two-dimensional Fourier transform (FFT) of the streamwise velocity fluctuations $u'(x,t)$ was used to identify the dominant propagating instabilities and their speeds.

$$\frac{1}{MN}\sum_{x=1}^{M} \mathrm{e}^{-j\,2\pi f_x x/M} \sum_{t=1}^{N} u'(x,t)\,\mathrm{e}^{-j\,2\pi f t/N} \qquad (3)$$

The temporal frequency is given by $St_0 = f\,\theta_{\text{sep}}/U_{\text{sep}}$ and spatial frequency by $k\,\delta^*_{\text{sep}} = 2\pi f_x\,\delta^*_{\text{sep}}$. Where δ^* is the boundary layer displacement thickness. At $Ma = 0.95$, δ^* and θ at the shock

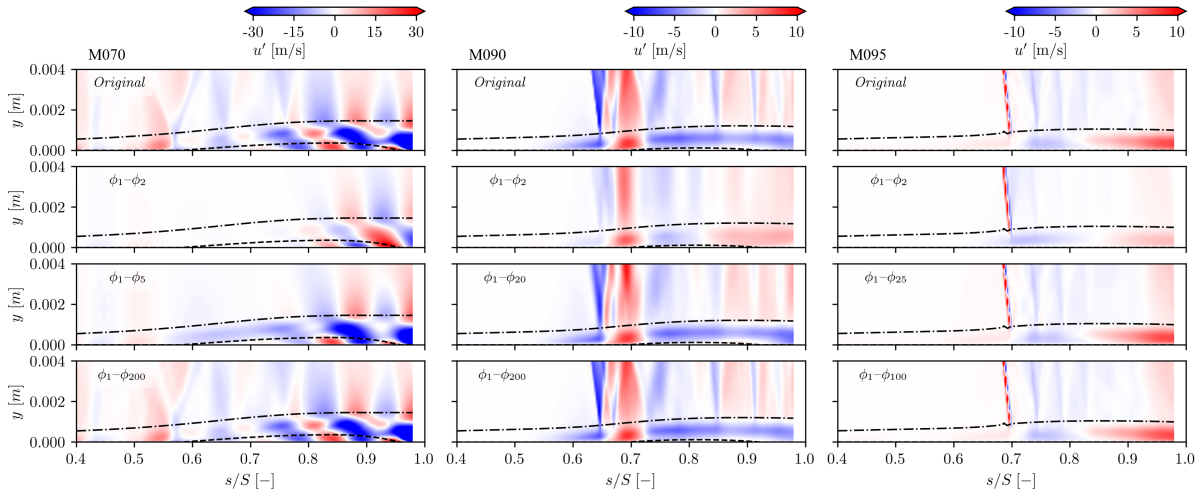

Figure 8: Low-rank reconstructions of instantaneous streamwise velocity fluctuations for $Ma = 0.70$, 0.90, and 0.95 using increasing numbers of POD modes. The dashed line highlights the edge of the recirculating region. The dot-dashed line represents the shear layer thickness.

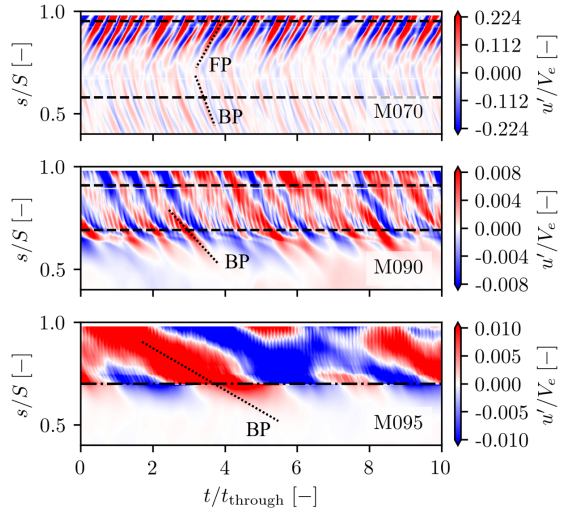

Figure 9: Time–space diagram of normalized u' at fixed wall-normal distance for Ma = 0.70, 0.90, and 0.95. The boundary layer edge velocity is used for normalization.

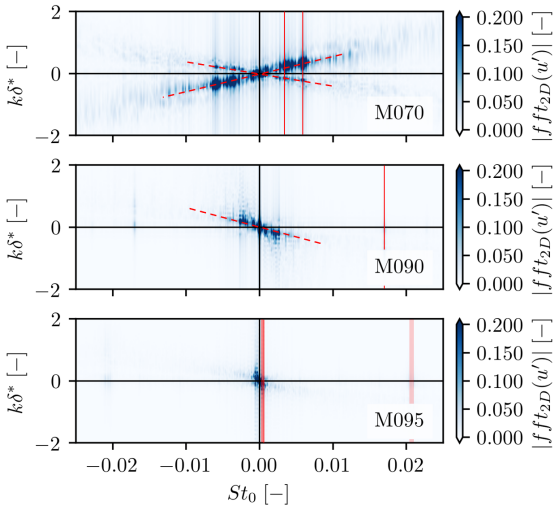

Figure 10: Amplitude of the 2-D Fourier transform of u' for $Ma = 0.70$, 0.90, and 0.95. Forward-leaning ridges indicate convective Kelvin–Helmholtz instabilities; backward-leaning ridges indicate upstream acoustic waves; vertical traces mark trailing-edge shedding or shock modulation.

foot are used. The speed of the propagating instability is obtained as:

$$\frac{U_{inst}}{U_{out}} = \frac{1}{2\pi U_{sep}} \frac{k\delta^*_{sep}}{St_0} \frac{\theta_{sep}}{\delta^*_{sep}} \tag{4}$$

The two-dimensional FFTs displayed in Figure 10 highlight that at $Ma = 0.70$, a forward-convective ridge in the first and third quadrants corresponds to the shear layer roll-ups traveling at $U_{\text{inst}} \approx 0.36 U_{\text{out}}$, with a symmetric backward-leaning ridge marking upstream acoustic waves, suggesting their coupling as a feedback loop. At $Ma = 0.90$ only the backward ridge appears, together with a vertical trace at $St_0 = 0.0170$ denoting trailing-edge shedding. At $Ma = 0.95$, vertical traces dominate, indicating non-convective unsteady shock modulation alongside a weak upstream acoustic ridge. The two vertical ridges at low $St_0 = 0.0003$ and 0.0006, characterize the low-frequency shock modulation. A broadband is identified near $St_0 = 0.021$. This feature, first identified in Figure 5, is associated with the trailing shed vorticity. A weak backward propagating ridge is also present.

Table 3 lists Strouhal number St_0, non-dimensional wavenumber, and instability speed

$U_{\mathrm{inst}}/U_{\mathrm{out}}$. At $Ma = 0.70$ the forward-propagating instabilities travel at 0.34–0.40U_{out}, matching the 0.30–0.60 range in Boutilier and Yarusevych (2012) and Pröbsting and Yarusevych (2014). The St_0 in the range 0.003–0.007 also agrees with the results of Dellacasagrande et al. (2024). At $Ma = 0.90$ and 0.95, only the backward (acoustic/shock) and vertical ridges remain. The vertical ridges occur at the trailing edge shed frequency and the shock modulation frequencies for the higher Mach number case. The values for the higher Mach number cases are reported in Table 3 for completeness.

Case	St_0	$k\delta^*$	U_{inst}/U_{out}
M070	0.0034	0.278	0.34
	0.0060	0.416	0.40
	0.0060	-0.208	-0.79
M090	0.0026	-0.223	-0.31
	0.0170	–	–
M095	0.0003	-0.069	-0.11
	0.0006	–	–
	0.0210	–	–

Table 3: Parameters of propagating instabilities.

7 Conclusions

Direct numerical simulations of the SPLEEN C1 cascade at $Re_c = 70{,}000$ reveal three distinct suction side regimes as outlet Mach increases from 0.70 to 0.95. At Ma = 0.70, a Kelvin–Helmholtz convective instability causing shear layer roll-ups is responsible for forward-propagating instabilities (convecting at $U_{\mathrm{inst}} \approx 0.36$–$0.40\,U_{\mathrm{out}}$) and matching upstream acoustic waves ($St_0 \approx 0.0034$–0.0060), reinforcing the feedback loop between the shear layer and acoustic. At Ma = 0.90, only backward-propagating ridges appear at $St_0 = 0.0169$, which are tied to trailing edge vortex shedding. The low-rank reconstruction shows that 20 POD modes suffice to reconstruct both bubble modulation and upstream-traveling acoustic waves. At Ma = 0.95, vertical FFT traces at low frequencies (0.85 and 1.6 kHz) indicate the passage shock modulation, with a weak acoustic ridge and five modes capturing the dominant shock dynamics.

The convective speeds, Strouhal ranges, and POD mode counts highlight how shear layer instabilities, acoustic waves, and shock interactions each dominate distinct off-design flow regimes. Such distinct behaviors reinforce the need for high-speed LPT designs and control strategies that address each mechanism throughout the flight envelope. Finally, incorporating realistic inlet turbulence in future work is recommended, as turbulence may alter the growth of instability and acoustic propagation.

Acknowledgments

The present research benefited from computational resources made available on Lucia, the Tier-1 supercomputer of the Walloon Region, infrastructure funded by the Walloon Region under the grant agreement n°1910247. The authors thank the research centre Cenaero for making the computational code ArgoDG available for the study and acknowledge the contribution of Maxime Borbouse in making the DNS data available.

References

Boutilier, M. S. H. and Yarusevych, S. (2012), Separated shear layer transition over an airfoil at a low Reynolds number, *Phys. Fluids*, Vol. 24, 084105.

Borbouse, M., Lopes, G., Lavagnoli, S., Rasquin, M. and Hillewaert, K. (2025), Analysis of separation and transition on a novel high-speed low-pressure turbine cascade, in *Cambridge Unsteady Flow Symposium*, pp. 341–362, Springer, Cham.

Börner, M. and Niehuis, R. (2021), Dynamics of shock waves interacting with laminar separated transonic turbine flow investigated by high-speed schlieren and surface hot-film sensors, *J. Turbomach.*, Vol. 143, No. 5, 051010.

Chu, B. T. (1965), On the energy transfer to small disturbances in fluid flow (part I), *Acta Mech.*, Vol. 1, pp. 215.

Dellacasagrande, M., Barsi, D., Lengani, D., et al. (2024), Instability processes in short and long laminar separation bubbles, *Exp. Fluids*, Vol. 65, 109.

Hillewaert, K. (2013), Development of the discontinuous Galerkin method for high-resolution, large scale CFD and acoustics in industrial geometries, PhD thesis, University of Louvain.

Jones, L. E., Sandberg, R. D. and Sandham, N. D. (2010), Stability and receptivity characteristics of a laminar separation bubble on an aerofoil, *J. Fluid Mech.*, Vol. 648, pp. 257–296.

Lavagnoli, S., Lopes, G., Simonassi, L. and Torre, A. F. M. (2023), SPLEEN—High Speed Turbine Cascade–Test Case Database, Zenodo, Switzerland.

Lengani, D., Simoni, D., Ubaldi, M., Zunino, P. and Bertini, F. (2017), Analysis of the Reynolds stress component production in a laminar separation bubble, *Int. J. Heat Fluid Flow*, Vol. 64, pp. 112–119.

Marxen, O. and Henningson, D. S. (2011), The effect of small-amplitude convective disturbances on the size and bursting of a laminar separation bubble, *J. Fluid Mech.*, Vol. 671, pp. 1–33.

Pröbsting, S., Serpieri, J. and Scarano, F. (2014), Experimental investigation of aerofoil tonal noise generation, *J. Fluid Mech.*, Vol. 747, pp. 656–687.

Rossiter, A. D., Pullan, G. and Melzer, A. P. (2023), The influence of boundary layer state and trailing edge wedge angle on the aerodynamic performance of transonic turbine blades, *J. Turbomach.*, Vol. 145, No. 4, 041008.

Sirovich, L. (1987), Turbulence and the dynamics of coherent structures, parts I–III, *Q. Appl. Math.*, Vol. 45, No. 3, pp. 561–590.

Uzun, A., and Malik, M. R. (2021). Simulation of a turbulent flow subjected to favorable and adverse pressure gradients. *Theoretical and Computational Fluid Dynamics*, 35(3), 293-329.